Using satellite rainfall products to assess the triggering conditions for hydro-morphological processes in different geomorphological settings in China

Nan Wang [a,b], Luigi Lombardo [c], Stefano Luigi Gariano [d], Weiming Cheng [a,b,e,f,*], Changjun Liu [g], Junnan Xiong [a,h], Ruibo Wang [a]

[a] *State Key Laboratory of Resources and Environmental Information Systems, Institute of Geographic Sciences and Natural Resources Research, Chinese Academy of Sciences, Beijing 100101, China*
[b] *University of Chinese Academy of Sciences, Beijing 100049, China*
[c] *University of Twente, Faculty of Geo-Information Science and Earth Observation (ITC), PO Box 217, Enschede AE 7500, Netherlands*
[d] *CNR IRPI, Research Institute for Geo-Hydrological Protection, Perugia 06127, Italy*
[e] *Jiangsu Center for Collaborative Innovation in Geographic Information Resource Development and Application, Nanjing 210023, China*
[f] *Collaborative Innovation Center of South China Sea Studies, Nanjing 210093, China*
[g] *China Institute of Water Resources and Hydropower Research, Beijing 100038, China*
[h] *School of Civil Engineering and Architecture, Southwest Petroleum University, Chengdu 610500, China*

ARTICLE INFO

ABSTRACT

Hydro-morphological processes (HMP, i.e. all processes contained within the spectrum defined between debris flows and flash floods) initiate in response to intense rainfall events. Efficient HMP hazard assessment over large regions is often hindered because of limited rainfall observations over mountainous areas. Real-time and easily accessible satellite rainfall products offer new opportunities to address the observational coverage problem in ungauged catchments. In this work, two satellite rainfall products, Global Precipitation Measurement (GPM) and Climate Hazards Group Infrared Precipitation with Station Data (CHIRPS), are investigated by taking the ground measurements as a reference. Based on a close agreement between GPM and rain gauge data, daily rainfall together with a series of antecedent rainfall values were calculated to investigate the spatio-temporal distribution of HMP occurred from 2001 to 2015 across the whole Chinese territory. Ultimately, rainfall thresholds for HMP initiation within different geomorphological settings in China were obtained by: (1) building antecedent rainfall sequences consisting of HMP and non-HMP via 100 nonparametric bootstrapped replicates; (2) testing several percentiles of the rainfall distribution as thresholds for HMP occurrence; (3) optimizing rainfall thresholds for six geomorphological macro-regions in China. This study confirmed the ability of satellite data in defining the rainfall conditions for the triggering of HMP, acknowledging the potential underestimation and/or bias that characterize any satellite rainfall products. Our findings provides new insight on rainfall conditions responsible for HMP initiation at the Chinese national scale.

1. Introduction

Intense rainfall prompts the challenges of hazard management for hydro-morphological processes (HMP), whose occurrence is increasing both in space and time under climate change (Seneviratne et al., 2012). A HMP is here considered as any process contained within the spectrum defined between flash floods and debris flows. Specific differences of the triggered phenomena within this spectrum depend on several factors,

among which the hydrological, geomorphological, and lithological properties of the landscape under consideration, the source material and the presence of sediments (Borga et al., 2014). China has widely experienced severe HMP in the last decades. They are triggered by large amounts of rainfall that can convert an otherwise normal event into an extraordinary, devastating disaster (Doswell et al., 1996).

Usually, the sparse distribution of rain gauge networks in particular in complicated topographic settings, which are particularly prone to

---

HMP, add further complexities in estimating the dynamics of extreme rainfall events (Creutin and Borga, 2003) and their cascading hazards. Therefore, determining the rainfall conditions responsible for HMP initiation - also in the form of rainfall thresholds - is challenging and yet, it is of paramount importance to plan preparatory/mitigation actions from destructive impacts, within rural settlements and urbanized areas (Scofield and Kuligowski, 2003).

Traditionally, defining rainfall thresholds for HMP initiation is mostly performed by using physically-based models (Norbiato et al., 2008; Miao et al., 2016). Despite the good performance these models offer, their operational use over large areas is limited by the required data (Hapuarachchi et al., 2011). Specifically, physically-based threshold models rely on the rainfall measurements and hydrological and geotechnical information that are usually not easily available in data-scarce catchments (Hapuarachchi et al., 2011). Similarly, these models rely on detailed soil properties (texture, hydraulic conductivity, cohesion and more; Bout et al., 2018), which can be acquired but at the cost of extremely expensive field surveys when the territory under examination extends over regional to national and continental scales.

Over large areas, an alternative to physically-based models can be implemented by adopting empirical methods (e.g. Borga et al., 2014; Schlögel et al., 2020), mostly with the aim of defining empirical rainfall thresholds (e.g. Badoux et al., 2012; Abancó et al., 2016; Bezak et al., 2016). Once the spatio-temporal rainfall distribution is retrieved, usually from rain gauges, it is possible to use long historical HMP records and derive rainfall thresholds (Miao et al., 2016), upon which alert levels are possibly issued from governmental agencies to inform the population of potential threats. In ungauged basins and data-scarce areas, satellite-based rainfall products are necessary (Gao et al., 2017). The latter are also useful to overcome several problems that hampers the capability of meteo-hydrological networks to catch hydrological conditions able to trigger HMP (Borga et al., 2014; Nikolopoulos et al., 2014; Nikolopoulos et al., 2015). Satellite-based rainfall products are also employed to build up early warning systems (Hong et al., 2007; Kirschbaum et al., 2015; Kirschbaum and Stanley, 2018; Chikalamo et al., 2020; Hartke et al., 2020). Recently, satellite-based rainfall products were also used to calculate rainfall thresholds for landslide and debris flows initiation at various spatial scales (Nikolopoulos et al., 2017; Brunetti et al., 2018; Monsieurs et al., 2019; He et al., 2020; Jia et al., 2020). In particular, He et al. (2020) defined several rainfall thresholds for landslide triggering in China (i.e., rainfall event-duration, normalized, for rainy and non-rainy periods, and for short and long rainfall durations) using: (i) 771 landslide events occurred in the period 1998–2017; and (ii) satellite-based rainfall products.

Among the currently available options, several satellite rainfall products have already been reported to perform well in estimating rainfall on increasing temporal scales, such as:

1. the Global Precipitation Climatology Project one-Degree-Daily (GPCP-1DD, 1996-present, 1°/ 1d; Huffman et al., 1997; Huffman et al., 2001);
2. Precipitation Estimation from Remotely Sensed Information using Artificial Neural Networks (PERSIANN, 1983-present, 0.25°/ 1d; Sorooshian et al., 2000);
3. Climate Prediction Center MORPHing technique (CMORPH, 1998-present, 0.07°/ 30 min; Joyce et al., 2004);
4. Global Satellite Mapping of Precipitation (GSMap, 2000-present, 0.1°/ 30 min; Kubota et al., 2007);
5. Tropical Rainfall Measurement Mission (TRMM, 1998-present, 0.25°/ 3 h; Huffman et al., 2007) and its successor
6. Global Precipitation Measurement (GPM, 2014-present, 0.1°/ 30 min; Hou et al., 2014);
7. Climate Hazards Group Infrared Precipitation with Stations (CHIRPS, 1981-present, 0.05°/ 1d; Funk et al., 2014; Funk et al., 2015).

Each one of these rainfall products has already been tested in hydrometeorological applications (Ashouri et al., 2016; Toté et al., 2015; Yuan et al., 2019; Tang et al., 2020). And, among the ones listed above, researchers highly recommended to take advantage of TRMM/GPM and CHIRPS datasets in hydro-morphological disaster forecasting (Fang et al., 2019; Shen et al., 2020; Zhou et al., 2020) because of the close match with ground rainfall observations. These two products (TRMM/GPM and CHIRPS) not only have a high spatial and temporal resolution but they also span over relatively long periods (Tang et al., 2020). These characteristics make them suitable to be analyzed together with HMP records in a historical context.

Although the available GPM products have been extended to June 2000, the evaluations on their agreement with rain gauge observations are mostly conducted based on recent datasets. For instance, comparisons carried out in mainland China confirmed the ability of GPM products in detecting the precipitation in humid regions, or southern China (Jiang and Bauer-Gottwein, 2019; Zhou et al., 2020). Similarly, the assessments on the long-term CHIRPS rainfall products have also been verified, especially indicating a close relationship with monsoon patterns in China (Bai et al., 2018) and in India (Gupta et al., 2020). Similar comparisons and analysis were made (e.g.) in Italy (Rossi et al., 2017) and in Brazil (Salles et al., 2019), providing satisfying results. Besides, the systematic negative biases of CHIRPS observed in some global analyses was effectively removed from 2000 onwards (Shen et al., 2020).

Determining rainfall thresholds for HMP is of paramount importance for operational prediction in hazard and risk management, and particularly in China. To address this issue, a methodology to detect preliminary rainfall triggering conditions for HMP by exploiting regional antecedent rainfall derived from satellite rainfall products is here proposed. Initially, we calculate several extreme rainfall indices and compare them with the rain gauge derived values. Then, on the basis of the satellite product which has shown the highest degree of accuracy with respect to ground measurements, we also compute current daily rainfall and a series of antecedent rainfall values (as made by e.g. Glade et al., 2000; Kirschbaum and Stanley, 2018) in different geomorphological settings across China. Ultimately, we derive preliminary rainfall thresholds for HMP initiation on the basis of statistically-based performance metrics.

For the first time, this work aims at taking full advantage of the satellite rainfall products and unique long-term historical HMP records, making it possible to derive preliminary rainfall thresholds for HMP initiation at the scale of the whole Chinese territory.

2. Study area and data sources

2.1. Study area

China approximately covers an area of 9.6 million km², and the mountainous area accounts for approximately 67% of its territory, with a marked increase in elevation from East to West. The rainfall features are greatly influenced by the East Asian Summer Monsoon, resulting in rainy seasons being concentrated between June and August across the Eastern and Central China. The arid to semi-arid climate affects the northwest China, which consist of desertic areas, suffering from droughts more often than other regions. Ultimately, the Tibetan Plateau is locally referred to as the Asian Tower, due to its prominent orographic features and represents one of the most complex topographic sectors of China.

The vast Chinese territory is characterized by various geomorphological settings, which can be classified into six main geomorphic-regions (Fig. 1) encompassing eastern plains (EP), southeastern hills (SEM), north-central plateaus (NCP), southwestern mountains (SWM), northwestern basins (NWB), and Tibetan Plateau (TP) according to the classification proposed by Wang et al. (2020). This classification is related to a combination of plate tectonics, crustal features,
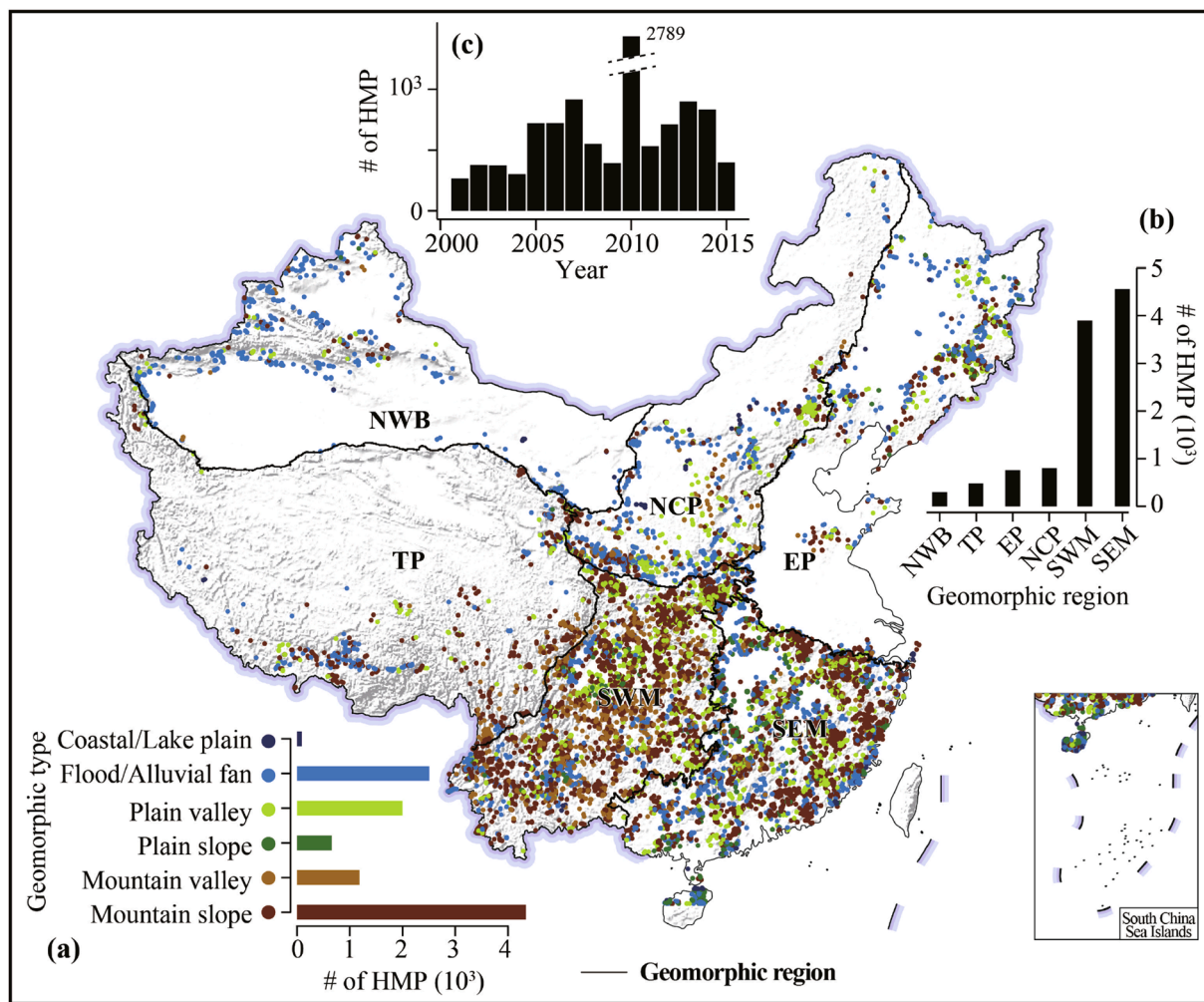
Fig. 1. Distribution of HMP across the Chinese six geomorphic-regions (key: EP, eastern plains; SEM, southeastern hills; NCP, north-central plateaus; SWM, southwestern mountains; NWB, northwestern basins; TP, Tibetan Plateau). Colored dots in the map correspond to geomorphic characteristics of the area where the HMP were recorded. Inset (a) reports the number of HMP per geomorphic type. Inset (b) reports the number of HMP per region. Panel (c) reports the number of HMP per year.

geomorphological features, and regional differences also including geomorphological types. To cope with the complexity of hydro-climatic and geomorphological settings over entire China, we proposed to adopt the subdivision into the six geomorphic-regions by taking full advantage of its generalization on the localized terrain and weather conditions. From South-East to North-West, the distance to sea together with orography and terrain characteristics contribute to forming the weather patterns in China, such as 200 mm, 400 mm, and 800 mm rainfall contours (Fig. 2). Therefore, the geomorphic-regions represent the best combination for reflecting the spatial similarity and difference among the weather conditions, terrain features, and also population distributions.

2.2. Hydro-morphological processes' inventory

The HMP inventory analyzed in this study is part of a national-scale collection coordinated by the Chinese Institute of Water Resources and Hydropower Research (Liu et al., 2018). This project was carried out with the purpose of collecting long-term information on HMP disasters in the period from 1950 to 2015.

To keep the information consistent with the time span of the satellite rainfall products, we only selected the recentmost records since 2001 and until 2015, from the entire HMP Chinese catalogue. Each HMP record is associated with information including the precise location

(longitude and latitude) and the date of occurrence (day, month and year) of the HMP. Overall, we extracted 15,636 HMP within the 15-year period under examination across the whole Chinese territory (Fig. 1).

2.3. Rainfall dataset

2.3.1. Rain gauge data

We used daily rainfall measurements recorded by meteorological stations in the same period 2001–2015. The daily rainfall were accessed via the China Meteorological Administration website (http://data.cma. cn/). After filtering out missing records (due to the weather or other factors), out of 839 weather stations distributed over China we selected 806 with complete records, which we then used to evaluate the rainfall estimates related to GPM and CHIRPS (Fig. 2). Besides, due to the difference in data sources, there is latent time gap between ground measurements (Beijing time) and satellite estimates (UTC time) which we accounted for in a pre-processing phase. We followed the criterion proposed by Fang et al. (2019) and by Zhou et al. (2020) to re-align the exact times among rainfall estimates.

2.3.2. GPM IMERG data

Global Precipitation Measurement (GPM), which was launched in February 2014 as the successor of the Tropical Rainfall Measuring Mission (TRMM), offers three global precipitation products: the Early,
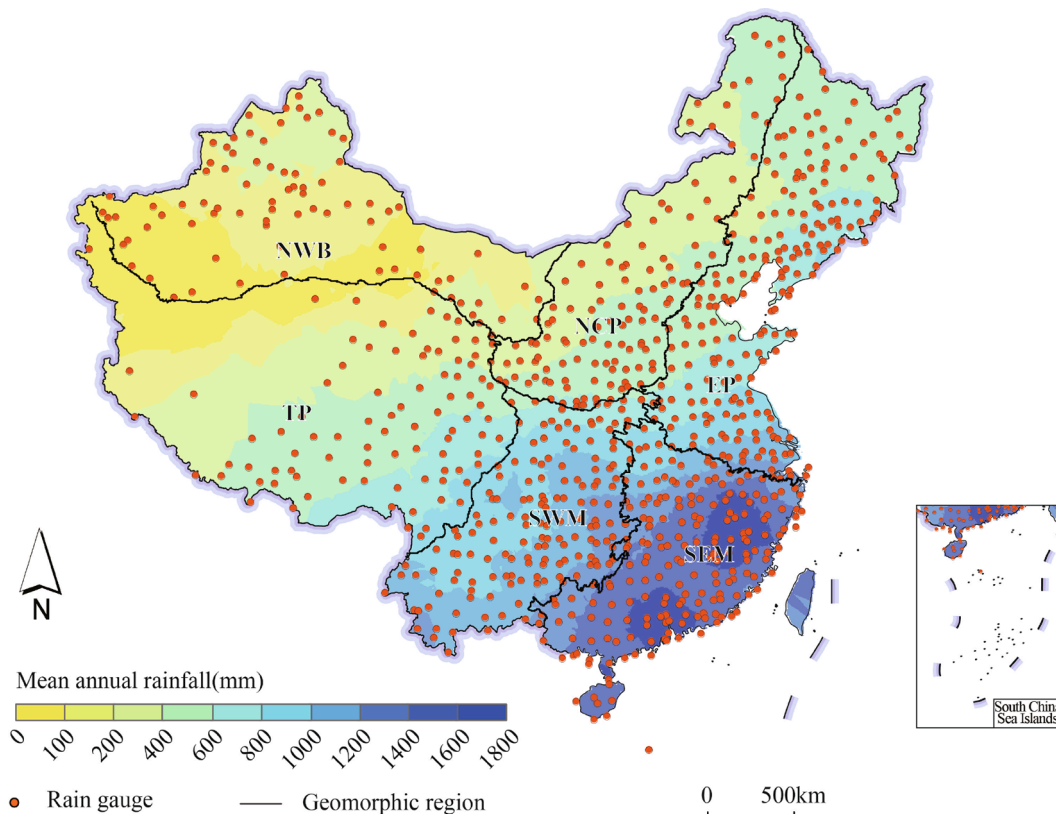
Fig. 2. Map of the mean annual rainfall in China overlaid by the rain gauge distribution and the boundaries of six geomorphic-regions (key: EP, eastern plains; SEM, southeastern hills; NCP, north-central plateaus; SWM, southwestern mountains; NWB, northwestern basins; TP, Tibetan Plateau).

Late, and Final Run (Huffman et al., 2015). The GPM products cover a spatial range of 60° S and 60° N, with a spatial resolution of 0.1° × 0.1°, and temporal resolution of 30 min. Among the three products, the Final Run product is considered to be more accurate because it features a monthly gauge bias calibration (Su et al., 2019; Sungmin et al., 2017). It has been widely used in the hydro-morphological researches showing satisfactory results (Wang et al., 2017). Therefore, we selected the Final Run data over China from 2001 to 2015, which can be obtained from NASA website (https://pmm.nasa.gov/data-access/downloads/gpm).

2.3.3. CHIRPS data

Climate Hazards Group Infrared Precipitation with Station Data (CHIRPS) offers the global precipitation estimations with daily, pentadal, and monthly products. CHIRPS is blended from multiple sources including rain gauge data and various satellite-based products. CHIRPS products are available since 1981 with two levels of spatial resolutions, 0.05° and 0.25°, respectively. We selected the 0.05° × 0.05° daily CHIRPS dataset covering the whole Chinese territory with a time span of 15 years, from 2001 to 2015. This can be accessed at https://www.chc.ucsb.edu/data/chirps.

3. Indicators and method

Three consecutive steps were defined and followed for the assessment and use of the satellite rainfall products. Initially, we made an assessment on GPM and CHIRPS products by comparing them with the daily rainfall data obtained from the ground measurements. Then, we compared the extreme rainfall obtained from the two satellite datasets with those from the rain gauge measurement. Ultimately, in light of the evaluation above, we derived the rainfall triggering conditions for HMP with the calculation of a series of antecedent rainfall in various geomorphic-regions.

3.1. Statistics metrics

The evaluation of the consistency between daily rainfall data derived via satellite estimates and ground measurements is crucial in such applications (Rossi et al., 2017; Gupta et al., 2020; Schlögel et al., 2020). This issue was examined by calculating four statistical indicators, including the Pearson correlation coefficient (CC), mean absolute error (MAE), root-mean-square error (RMSE), and relative bias (RB). Table 1 lists the equations of the statistics indices.

We used the Hanssen-Kuipers (HK; Hanssen and Kuipers, 1965) skill score to discriminate the rainfall thresholds in this study. HK skill score is based on the combination of different realizations between observations and predictions defined in a common confusion matrix (including true positives, TP; true negatives, TN; false positives, FP; and false negatives, FN; Fawcett, 2006), being defined as a linear combination of true positive rate (TPR) and false positive rate (FPR) (Stephenson, 2000; Wilks, 2011), according to the following equation:.

$$HK = TPR - FPR = \frac{TP}{TP + FN} - \frac{FP}{TN + FP} \tag{1}$$

It ranges from −1 to 1, with 1 indicating a perfect performance and

Table 1
Definitions and equations of the statistics indices.

Indicator	Acronym	Equation	Unit
Correlation Coefficient	CC	$CC = \frac{\sum_i^n (X_i - \overline{X})(Y_i - \overline{Y})}{\sqrt{\sum_i^n (X_i - \overline{X})^2}\sqrt{\sum_i^n (Y_i - \overline{Y})^2}}$	–
Mean Absolute Error	MAE	$MAE = \frac{\sum_i^n (Y_i - X_i)}{\sum_i^n X_i} \times 100$	mm
Root Mean Square Error	RMSE	$RMSE = \sqrt{\frac{\sum_i^n (Y_i - X_i)^2}{n}}$	mm
Relative Bias	RB	$RB = \frac{Y_i - X_i}{X_i} \times 100$	%

−1 representing very poor performance.

3.2. Extreme rainfall

The detection and analysis of rainfall extremes are necessary for studying their spatial and temporal prediction (e.g. Schlather, 2002; Saunders et al., 2017) and vital for HMP prediction (Borga et al., 2014; Nikolopoulos et al., 2017). In our case, it can be estimated by comparing the distribution of extreme rainfall indices detected from satellite-based products and ground measurements. A number of suggestions have already been indicated by the World Meteorological Organization to assess extreme precipitation (Klein Tank et al., 2009). In this work, we selected several popular indices listed in Table 2.

3.3. Antecedent rainfall

To identify the rainfall conditions responsible for HMP initiation, the effective antecedent rainfall within a given time window (typically short) should be considered together with the induced variations in soil properties. We adopted the antecedent rainfall model proposed by Kohler and Linsley (1951) and obtained a series of values, corresponding to 1, 2, 3, 4, 5, 6, 7 days preceding any HMP record in our dataset. Below we report the equation we used:

$$AR_n = P_0 + kP_1 + k^2P_2 + \cdots + k^nP_n \tag{2}$$

where, AR_n indicates the cumulative rainfall over the n days before the occurrence of a HMP, P_i is the daily rainfall for the ith day before the HMP, and k is an empirical calibration constant with the range of 0.8 to 0.98 proposed by Viessman et al. (1989) and later tested in several studies (e.g., Filho et al., 2020). By applying a decaying constant value in the calculation of antecedent rainfall, this equation accounts for the water infiltration and evapotranspiration caused by soil permeability (Blanchard et al., 1981). Glade et al. (2000) proposed a similar method to calculate rainfall thresholds for shallow landslide initiation in New Zealand. Here, we set k at 0.9 in the light of researches performed in Chinese territory (Bai et al., 2014; Ma et al., 2014; Wei et al., 2008).

3.4. Rainfall thresholds

Rainfall thresholds based on antecedent rainfall were calculated for each of the six Chinese geomorphic-regions, considering that the regional distribution of HMP is also controlled by local terrain attributes, soil types, and climatic conditions. The partition into geomorphic-regions are confirmed to be associated with comprehensive interplay among topography, geomorphology, soil, vegetation, and climate (Wang et al., 2020).

The approach for determining the rainfall threshold values was contextually based on antecedent rainfall values related to HMP initiation and on antecedent rainfall values that are likely not related to HMP occurrence (non-HMP), according to the following steps.

Table 2
Definition of the rainfall indices used in this study.

Extreme indices	Acronym	Definition	Unit
Heavy rainfall days	R50	Count of days with rainfall ⩾50 mm	d
Maximum daily rainfall	R1d	Annual maximum daily rainfall	mm
Maximum 5-days rainfall	R5d	Annual maximum consecutive 5-days rainfall amount	mm
Rainfall on wet days	R90p	Annual total rainfall of rainy days with rainfall exceeding the 90th percentile	mm
Simple daily intensity index	SDII	Mean rainfall when daily rainfall > 1 mm	mm/d
Consecutive wet days	CWD	Maximum number of consecutive rainy days	d

- The construction of the non-HMP date list was implemented on the basis of disaster locations. By exploiting the whole spatiotemporal domain our HMP database cover, we selected dates when HMP were recorded but in a different year, when no HMP occurred.
- The non-HMP antecedent rainfall were calculated according to the aforementioned date list.
- The whole non-HMP antecedent rainfall sequence were integrated together with the actual HMP counterparts. Because the number of non-HMP instances are much larger than the HMP occurrences, we randomly subsampled the non-HMP cases with an equal number to the HMP ones. And, we repeated this procedure 100 times to create a robust number of bootstrap replicates to be used in the following procedure.
- We extracted the 2.5%, 25%, 50%, 75%, 97.5% percentiles of the rainfall distribution together with the mean value of the whole sequence and then tested these values as potential cutoffs to distinguish HMP from non-HMP.
- The evaluation was made in light of several statistics metrics, including sensitivity, precision, specificity, and accuracy (Green and Swets, 1966; Jollifee and Stephenson, 2003). The mean values estimated from the 100 iterations were used to assess the most reliable results and the associated uncertainty. The rainfall thresholds that performed the best with a highest hit rate amongst the antecedent rainfall series were determined to be the optimum thresholds.

4. Results

4.1. Daily rainfall

The daily rainfall series were obtained from both GPM and CHIRPS datasets, and compared against the rain gauge measurements, which has been used as the benchmark dataset throughout the analyses. In doing so, we explored the relationship between the daily rainfall recorded by rain gauges and satellites to evaluate their performance in estimating extreme rainfall events. Table 3 shows that GPM has a higher correlation coefficient (R = 0.66) than that of CHIRPS (R = 0.50), although it indicates a slight underestimation of daily rainfall with the MAE of 15.5 mm. GPM also shows a RMSE (7.03 mm) lower than CHIPRS's (9.15 mm). Besides, GPM outperformed CHIRPS with a slightly lower relative bias (RB = 6.61%). Our findings indicated an underestimation of both satellite products, in agreement with most of the previous studies (Bai et al., 2018; Fang et al., 2019; Shen et al., 2020; Su et al., 2019; Zhou et al., 2020).

Fig. 3 displays the spatial distribution of statistical metrics for daily rainfall across China. GPM and CHIRPS both showed to be highly consistent with respect to the rain gauge measurements in eastern sector, but GPM indicated a much higher correlation coefficient (Fig. 3a and Fig. 3e). The highest mean absolute error (MAE > 50 mm) between GPM and rain gauge observation are more likely to be distributed in central China (Fig. 3b); however, the highest MAE between CHIRPS and rain gauge measurements appears in the southeastern sector (Fig. 3f). The spatial distribution of RMSE displayed a similar pattern for both satellite-based datasets, with the value decreasing from southeast to northwest in China (Fig. 3e and Fig. 3g). Ultimately, the high value of relative bias appears to be randomly distributed over China with the most evident underestimation (RB < −80%) and overestimation (RB > 30%) both scattered in northwest China (Fig. 3d and Fig. 3h).

Table 3
Correlation between satellite rainfall products and ground measurements.

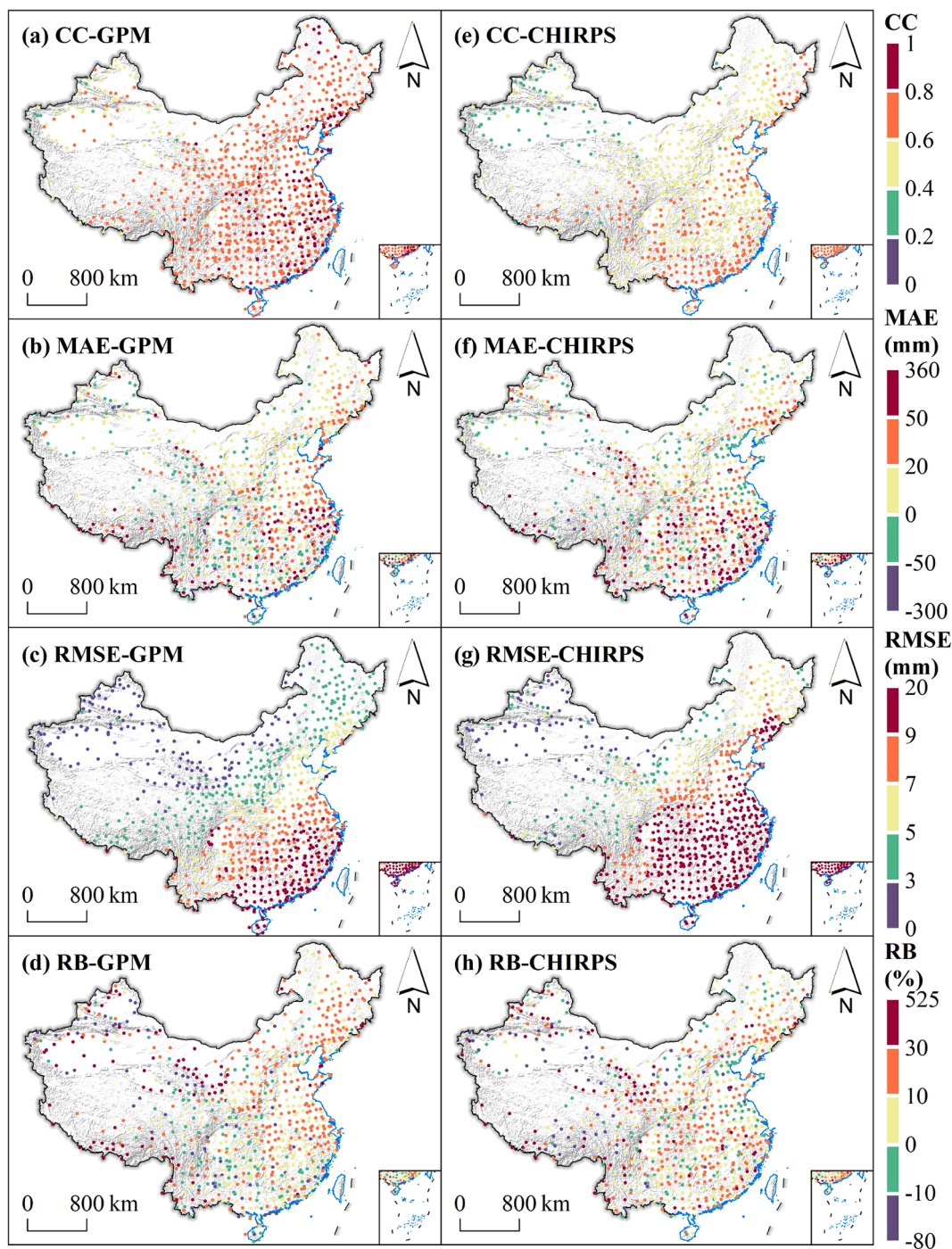| Statistical indicators	GPM	CHIRPS
CC	0.66	0.50
MAE (mm)	15.53	22.00
RMSE (mm)	7.03	9.15
RB (%)	6.61	9.56

Fig. 3. Spatial distributions of statistical metrics for daily rainfall derived from GPM (a-d) and CHIRPS (e-h) in China. Key: CC, correlation coefficient; MAE, mean absolute error; RMSE, root mean square error; RB, relative bias; see Table 1 for further explanations.

4.2. Extreme rainfall

A thorough comparison reveals the efficiency of satellite products with respect to ground measurements (here used as reference) in estimating extreme rainfall relevant to HMP (Fig. 4). Overall, both satellite products were in accordance with ground measurements, although GPM indicated a higher consistency with rain gauge observations. For most extreme indices, the GPM had the R value greater than 0.7, except for CWD. Besides, CHIRPS showed an obvious overestimation on R50 and R90p, and a relatively underestimation on SDII. Among all the extreme rainfall indices, GPM and CHIPRS are reported to perform best on estimating the R90p, where we also note a Pearson correlation of 0.945 and

0.927, respectively. GPM and CHIRPS showed limited correlations with rain gauge observations on estimating CWD, and the R values were found to be slightly larger than 0.5 for both of them.

Even though results from this study show some degree of bias for both satellite datasets on extreme rainfall prediction, this is a technical issue that can only be addressed by further improving the satellite-based products. Nevertheless, if we prove that even a slightly biased satellite-based rainfall product can be of use in estimating HMP thresholds, this could enable analyses even in ungauged regions and at a consistent spatial resolution. These two elements cannot be supported by rain gauge data because the weather station network is always irregularly distributed over space.
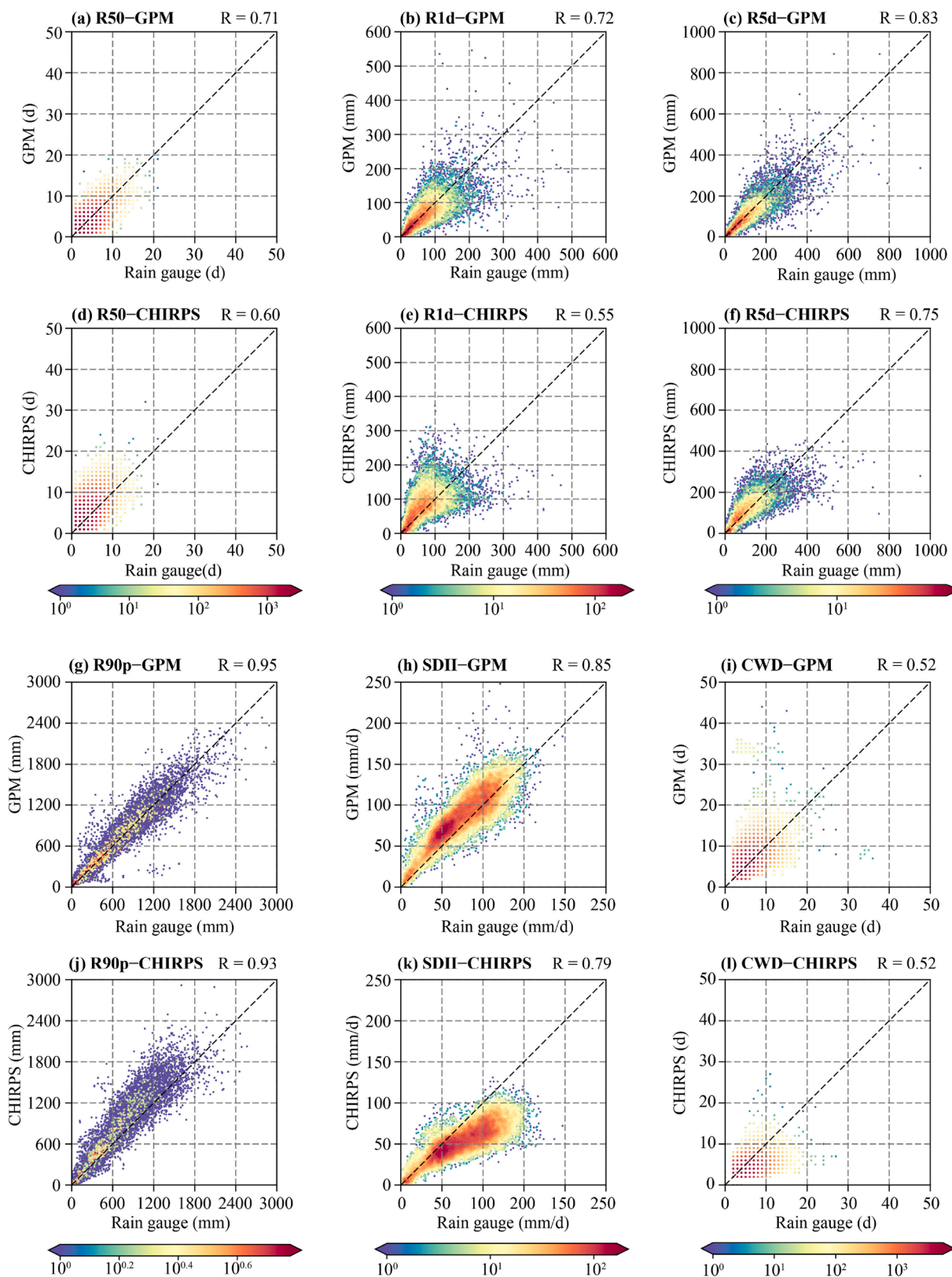
Fig. 4. Density-colored scatterplots of satellite-derived extreme rainfall indices (see Table 2) versus rain gauge observations. (For interpretation of the references to color in this figure legend, the reader is referred to the web version of this article.)

In the follow-up of this work, we will test the aforementioned hypothesis by estimating thresholds of HMPs using the GPM data, which provided better performance in detecting the extreme rainfall events compared to CHIRPS.

4.3. Current daily rainfall for HMP

As mentioned before, any assessment based on rain gauge observations is limited to regions equipped with densely distributed weather

stations. This is not often the case for area where HMP occurs, because of the mountainous landscape and the complex terrain settings. There has not yet been any inspection given on the satellite-derived rainfall and ground measurements based on the HMP locations. This study explores a potentially valid alternative to rain gauge data and associated uncertainties when deriving HMP thresholds. Specifically, to investigate the difference between the two datasets, we assessed satellite rainfall products versus the grid-interpolated rain gauge rainfall estimates.

Given that the gauges are sparsely-distributed in mountainous area, we applied an IDW interpolator to the ground observations and downsampled it over space to match the GPM resolution. The current daily rainfall at the HMP location was portrayed in light of the grid-interpolated rain gauge rainfall estimation in Fig. 5. The results indicated similar spatial pattern between rain gauge and GPM-derived daily rainfall, although a large difference exists in absolute value between the two. The high rainfall value are more likely to show up in regions between longitude of 105° to 120° E and latitude of 25° to 35° N. The interpolated daily rainfall, estimated via rain gauge observations, were much higher than the values derived from GPM product. The relative bias (RB) between these two datasets were portrayed with colored points to highlight that the majority of RB values were less than 100%. The higher RB is homogeneously distributed in central and southern China. This figure shows that for the vast majority of China, the differences between ground measurements and satellite-based rainfall estimates are approximated to a constant shift, thus making the two products almost linearly related one another.

4.4. Antecedent rainfall

The rainfall distribution patterns showed a large spatial differentiation in China due to the complex terrain and the various climatic regions. To better understand the localized causative factors for HMP occurrence, the antecedent rainfall with duration of 1, 2, 3, 4, 5, 6, and 7 days were calculated within six geomorphic-regions as well as six geomorphic types, respectively, and the probability density plots of antecedent rainfall are displayed in Fig. 6. For comparison, the daily rainfall for the current day of HMP is labeled as 0 days in the figure (the same for the following figures). Fig. 6a displays the current daily rainfall and antecedent rainfall related to HMP occurrences within each geomorphic-region. In doing so, we tested whether we could recognize the rainfall metric responsible for HMP occurrence, in distinct geomorphic-regions. Results showed that the current daily rainfall and the antecedent rainfall for the HMP occurrence were severe higher in the monsoon regions: SEM, SWM, and EP. While in NWB, most of its area is characterized as desert, showed the most extremely low amount of rainfall (lower than 50 mm) for the HMP occurrence. Moreover, the different geomorphic-regions displayed obviously different triggering rainfall patterns.

We further analyzed the current daily rainfall and antecedent rainfall related to HMP occurrences according to specific geomorphic types, including coastal/lake plains, flood/alluvial fan, mountain slope, mountain valley, plain slope, and plain valley. Here, the geomorphic types indicate the occurrence location of HMP categorized through the combination of general landscapes. This comparison information is supposed to assist the understanding of our choice of using geomorphic-regions as the final input. Fig. 6b displays the summary of the triggering rainfall patterns for HMP within each localized geomorphic unit. The highest current daily rainfall was associated with coastal/lake plain, followed by plain slope and mountain slope. However, HMP occurred in flood/alluvial fan and mountain valley were more likely to be induced
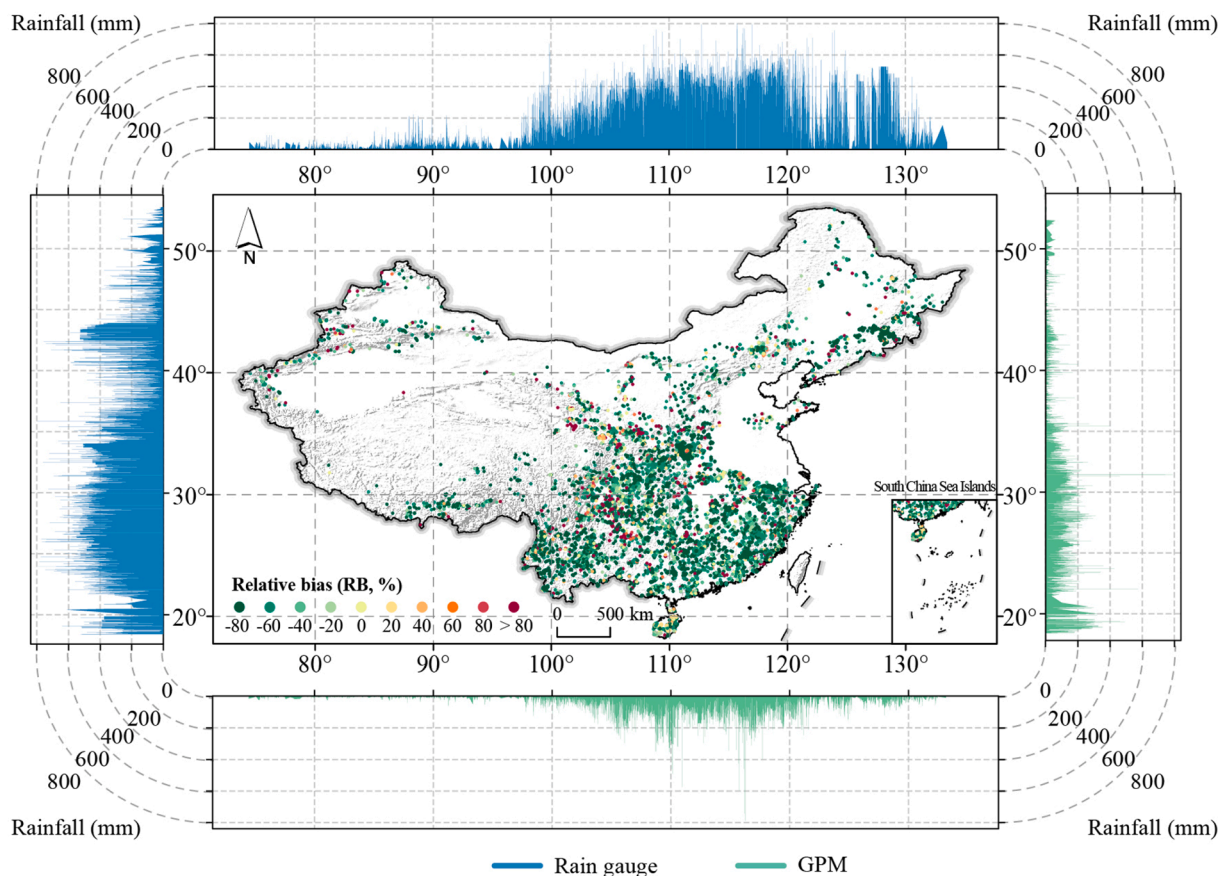

Fig. 5. Current daily rainfall (rainfall date extracted on the same date reported in the HMP catalogue) and its relative bias computed as the difference between rain gauge (blue) and GPM (green) data. (For interpretation of the references to color in this figure legend, the reader is referred to the web version of this article.)
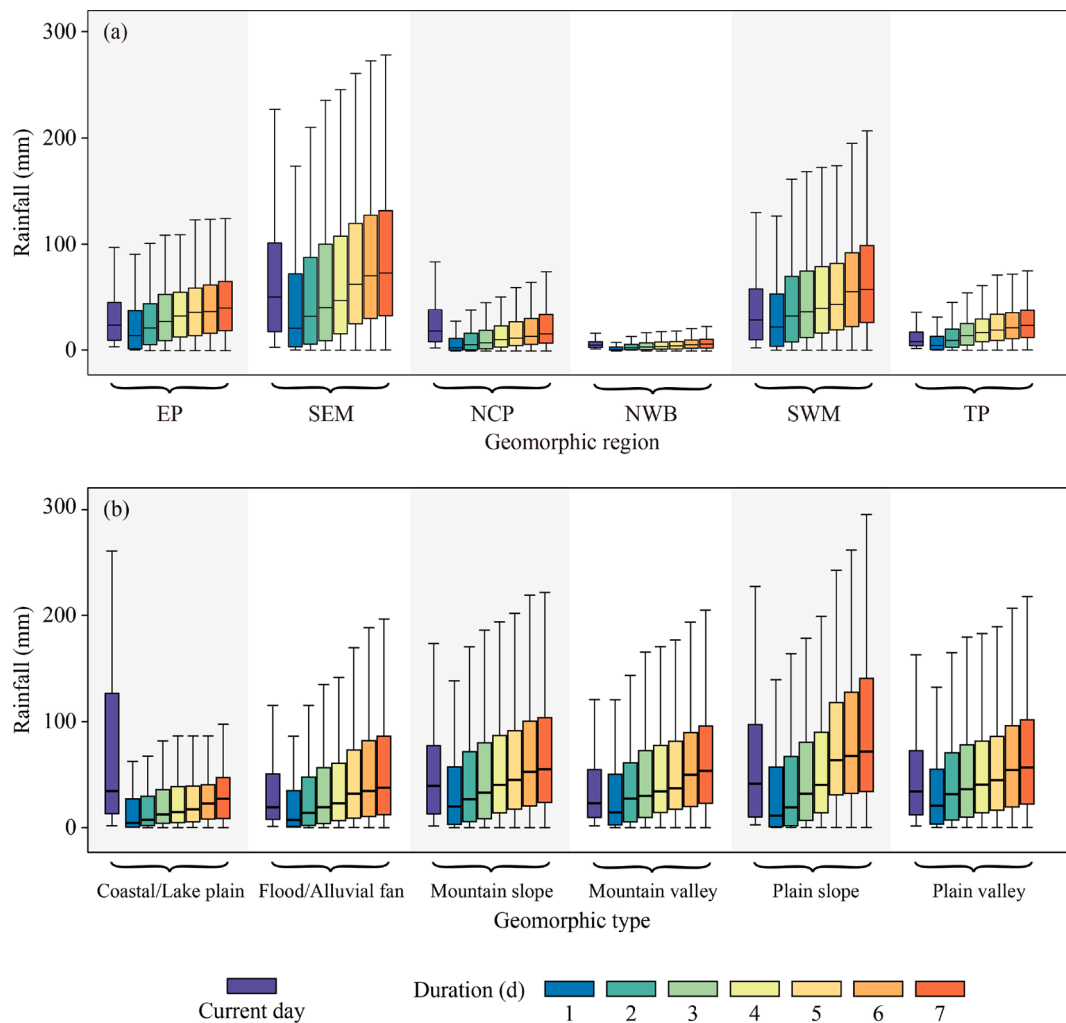
Fig. 6. Rainfall estimates extracted for each HMP and within each geomorphic types under consideration. The color scheme indicates the timespan considered for rainfall analysis: the rainfall in day of the HMP occurrence is indicated in purple; the other colors are associated with antecedent precipitation aggregated from 1 to 7 days before the date of the HMP occurrence. (For interpretation of the references to color in this figure legend, the reader is referred to the web version of this article.)

by a smaller amount of rainfall compared to the other geomorphic types. The figure also reveals different levels of variance for antecedent rainfall among the geomorphic types. For coastal/lake plain, the 1 to 7 days antecedent rainfall are all relative low, which are mostly lower than 50 mm. While, in plain slope, the continuously rainfall increase in at most 4-day before the occurrence of HMP together with the merely rainfall accumulation in the more previous stage was detected.

Fig. 7 displays the probability density plots of antecedent rainfall. The antecedent rainfall in SEM region can reach up to 700 mm, followed by SWM with a range of 0 to 500 mm. In EP, NCP, and TP regions, the maximum antecedent rainfall was detected to be less than 300 mm. However, the antecedent rainfall related to HMP initiation was merely less than 100 mm in NWB, which is recognized as the driest region in China. The probability density plots in Fig. 7 also illustrated a large variability of rainfall distributions across geomorphological sectors namely, from unimodal to bimodal as well as near-Gaussian to heavy-tailed shapes. For most of geomorphic-regions, the highest probability appeared between 0 to 100 mm. Notably, the 5 or more days antecedent rainfall in SEM and SWM indicated a second peak with the highest probability show up at 200 mm and 150 mm (Fig. 7b and Fig. 7e), respectively.

4.5. Rainfall thresholds for HMP

We then plot the current daily rainfall and antecedent rainfall series for HMP and non-HMP separately with the purpose of graphically distinguishing between the two situations. The most obvious difference in precipitation regimes between HMP presence (shown in orange) and absence (shown in green) conditions can be seen in the geomorphic-regions of EP, SEM, and SWM (Fig. 8a, Fig. 8b, and Fig. 8e). Here the interquartile ranges (the distance between the 75th and the 25th percentiles) of the presence and absence cases do not overlap. As for the NCP, NWB, and TP regions (Fig. 8c, Fig. 8d, and Fig. 8f), the situation is more complex. Here the distinction between rainfall amounts and the resulting presence or absence of HMP not straightforward because the main bulk of the rainfall distributions does overlap. This may imply, already from a simple graphical summary that a better performance of rainfall thresholds might be achieved for EP, SEM, and SWM rather than for NCP, NWB, and TP. Before testing this consideration through specific thresholds, we also included a complementary threshold-independent metric in our workflow. Specifically, we calculated the ROC curves (Receiver Operating Characteristic; Fawcett, 2006; Hosmer and Lemeshow, 2000; Amato et al., 2019) for each geomorphic-region. A ROC curve is a common performance evaluation tool for binary classifiers (Lombardo et al., 2020). The vector of presence/absence instances is compared to a vector of continuous values for which a large number of
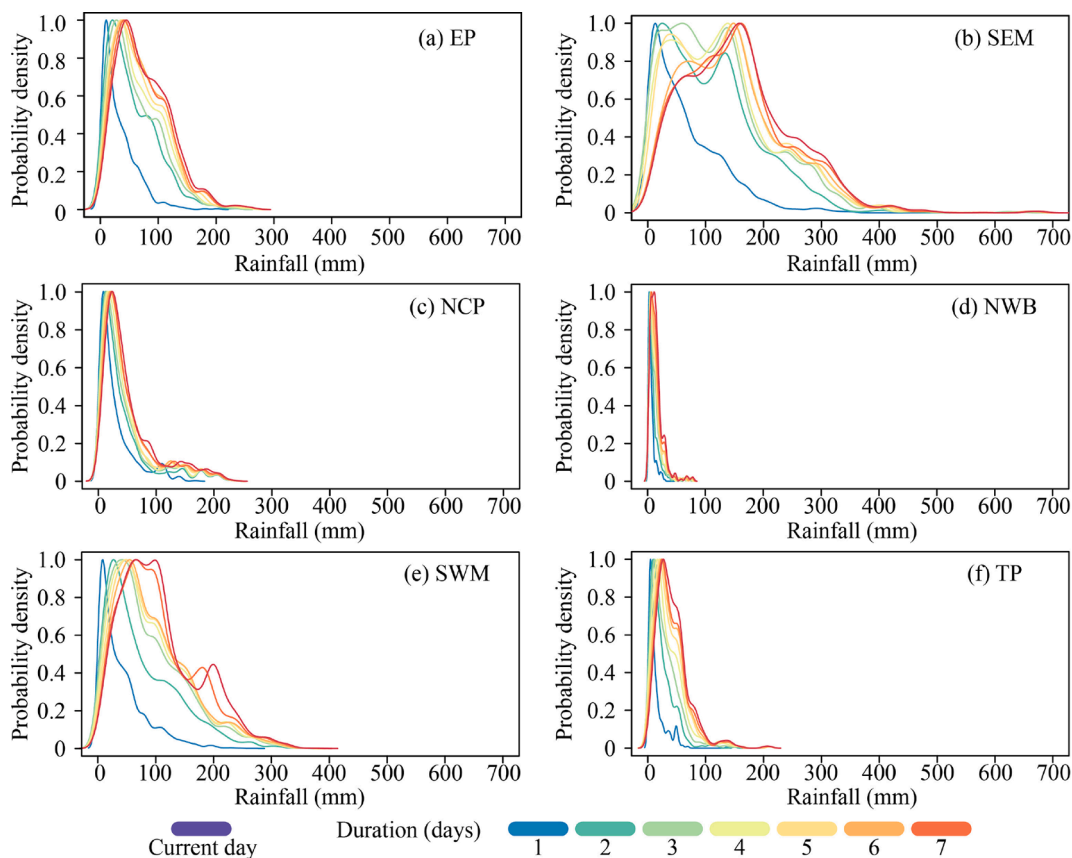
Fig. 7. Probability density plot of the antecedent rainfall of HMP in each of the six geomorphic-regions. Key: EP, eastern plains; SEM, southeastern hills; NCP, north-central plateaus; SWM, southwestern mountains; NWB, northwestern basins; TP, Tibetan Plateau.

thresholds is tested. For each considered threshold, the TPR and the FPR are computed, becoming the coordinate pair of each point in a ROC curve. As a result, the integral of this curve (or AUC for Area Under the Curve) measures the ability of a continuous estimate (here our rainfall) to match the presence/absence HMP conditions. AUC values nearing 1 are considered optimal and values nearing 0.5 indicate quite poor results (Lombardo and Mai, 2018).

In Fig. 9, with the exception of SWM, we show that the largest AUC values are achieved by considering the rainfall discharged the same day of the HMP occurrence. As for the SWM region itself, the best performance is achieved by considering one day before the event. This indication is quite reassuring in light of the following consideration. In rainfall threshold studies applied to landslides, a large antecedent period before the actual mass movement is a robust choice because the increase in pore pressure required to trigger the failure mechanism may actually span over several days, especially when the sliding surface is deep. However, for shallow processes such as those featured in our HMP catalogue, we expect the slope response to act on a much narrower time window.

Having tested the efficiency of satellite rainfall estimates in distinguishing HMP and non-HMP conditions over China, both graphically and via threshold-independent performance metrics, in the remainder of the manuscript we will focus on testing specific rainfall thresholds. To do so, we tested thresholds corresponding to five quantiles ($\tau_1 = 0.025$, $\tau_2 = 0.25, \tau_3 = 0.50, \tau_4 = 0.75$ and $\tau_1 = 0.975$) and the mean of the rainfall distribution for each of the six geomorphic-regions of China. For each of these six thresholds we then computed: sensitivity, precision, specificity, and accuracy, based on a classic contingency matrix (Rahmati et al., 2019). On the basis of the Pareto Efficiency criterion (see Tegmark and Wu, 2020, for further details), when both the higher TPR and lower FPR reach their optimal values, then the improvement of one

might result in the worsening of the other (Vrugt et al., 2003). In this work, to optimize the statistics indices, the satisfactory result are obtained when the threshold was set as the upper quantile ($\tau_4 = 0.75$) or mean of the rainfall distribution (Fig. 10). More specifically, in SEM and SWM, the threshold set at $\tau_4 = 0.75$ or mean value showed the notable difference between HMP and non-HMP with the four statistics indices, all greater than 0.8. The cutoffs worked best with 1-day antecedent rainfall for estimating rainfall thresholds in SEM and SWM. For EP, NCP, and NWB, the best performance for distinguishing HMP was found at $\tau_4 = 0.75$ or mean of current daily rainfall with the acceptable values of accuracies.

The most important parameter out of the four performance metrics is the sensitivity because it indicates the rate with which a binary classifier is able to estimate the presence conditions, or the HMP in our case. Therefore, we selected the 75% percentile or mean as our best rainfall threshold because they actually produce the highest sensitivity results as well as the acceptable other three indicators. In light of this consideration, the higher specificity and accuracy obtained by using larger thresholds such as the $\tau_1 = 0.975$ has less priority and we still favored the cutoff set at $\tau_4 = 0.75$ (or the mean itself).

To further clarify this concept, we use the HK skill score to directly interpret the performance of the rainfall thresholds (Fig. 11). When shifting the cutoff along with the distribution of HMP and non-HMP, for most geomorphic-regions, the best performance among all these combinations of antecedent rainfall sequence and quantiles are detected with $\tau_4 = 0.75$ and mean values. Meanwhile, the increase of the antecedent rainfall duration results in a general worsening of the HK skill scores. In SEM and SWM, the variance of HK skill score is not obvious, while the difference is much more evident in NCP and NWB. TP shows an exception with the best performance detected with 50% percentile of current daily rainfall (HK = 0.37).
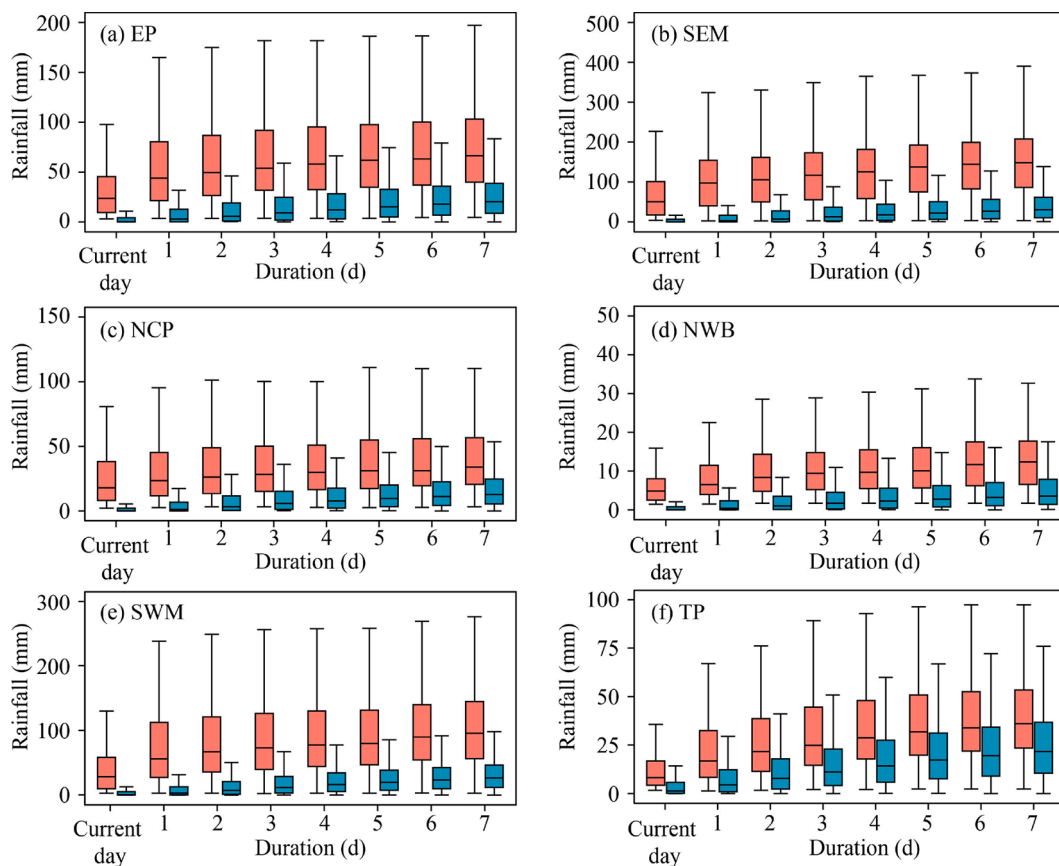
Fig. 8. Boxplot of the antecedent rainfall for HMP (orange bars) and non-HMP (green bars) events. Key: EP, eastern plains; SEM, southeastern hills; NCP, north-central plateaus; SWM, southwestern mountains; NWB, northwestern basins; TP, Tibetan Plateau. (For interpretation of the references to color in this figure legend, the reader is referred to the web version of this article.)
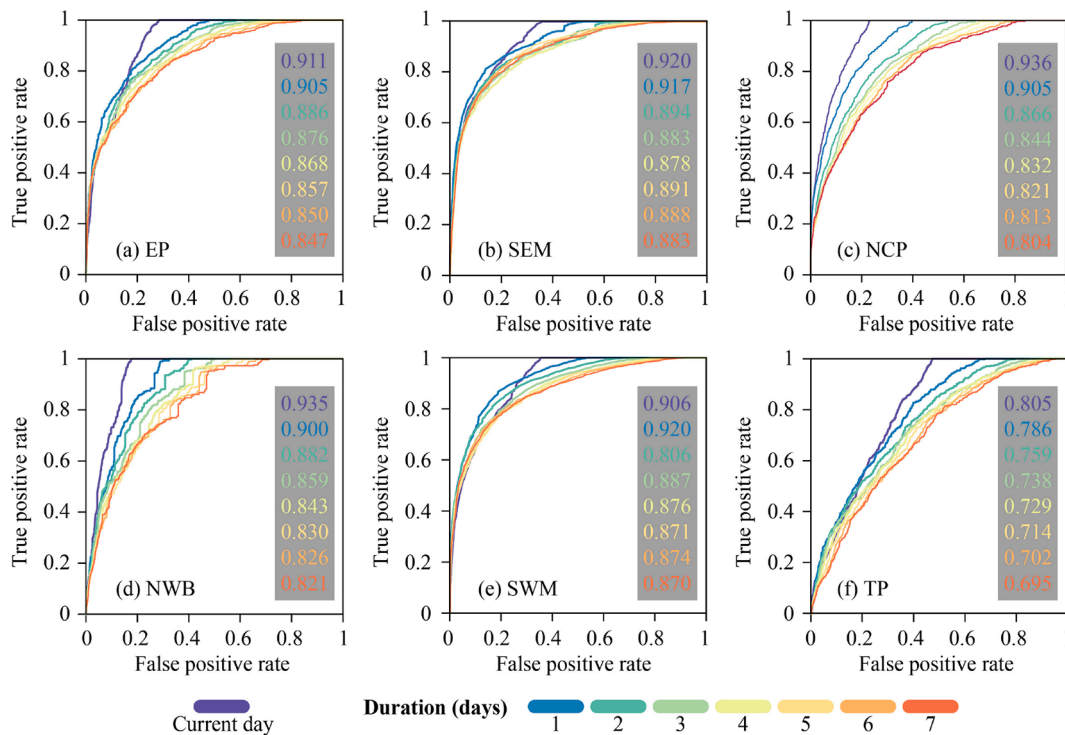

Fig. 9. ROC curves for the antecedent rainfall of HMP and non-HMP events, for the six geomorphological regions (key: EP, eastern plains; SEM, southeastern hills; NCP, north-central plateaus; SWM, southwestern mountains; NWB, northwestern basins; TP, Tibetan Plateau). The coloured values are the AUC values for each duration.
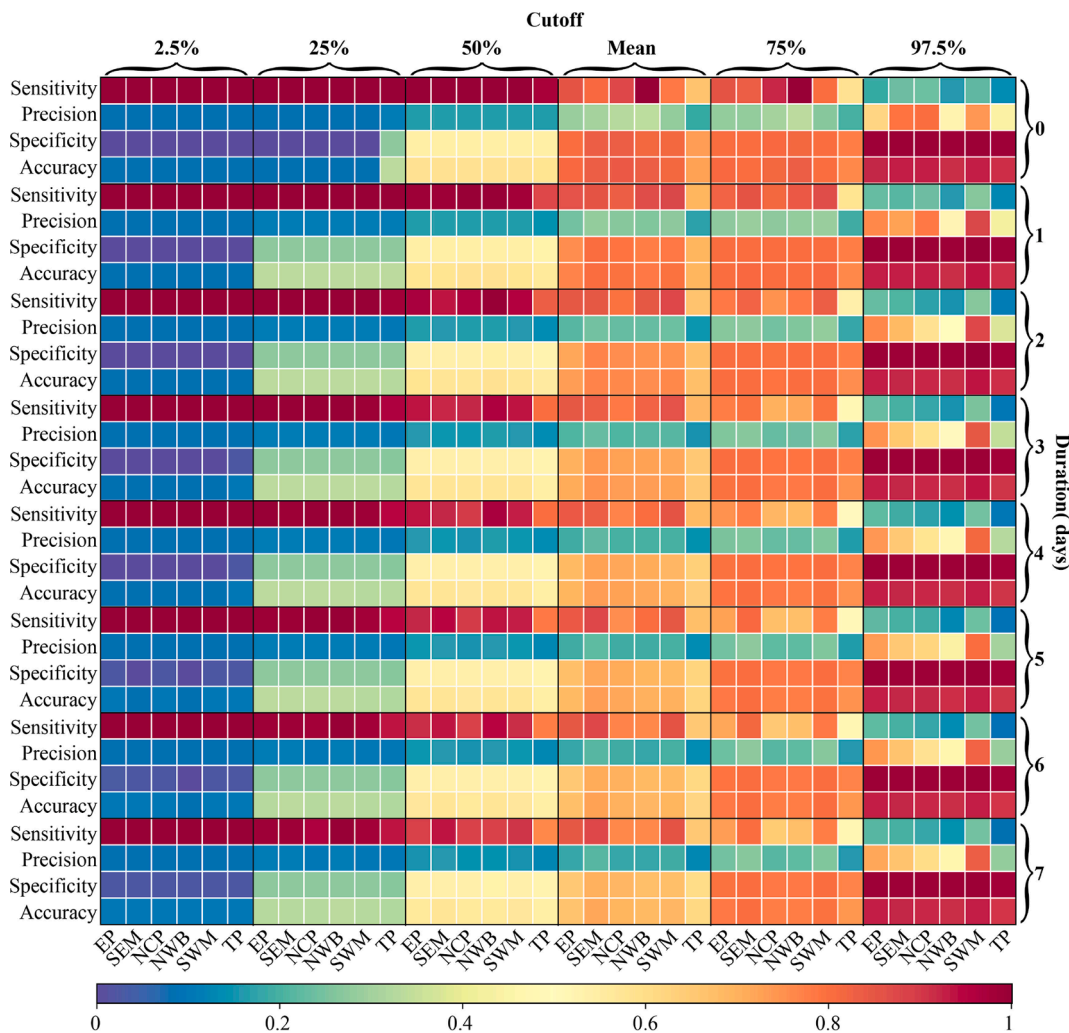
Fig. 10. Classification statistics matrix computed on the basis of rainfall thresholds (columns) selected by using current daily rainfall and antecedent rainfall sequence (rows).
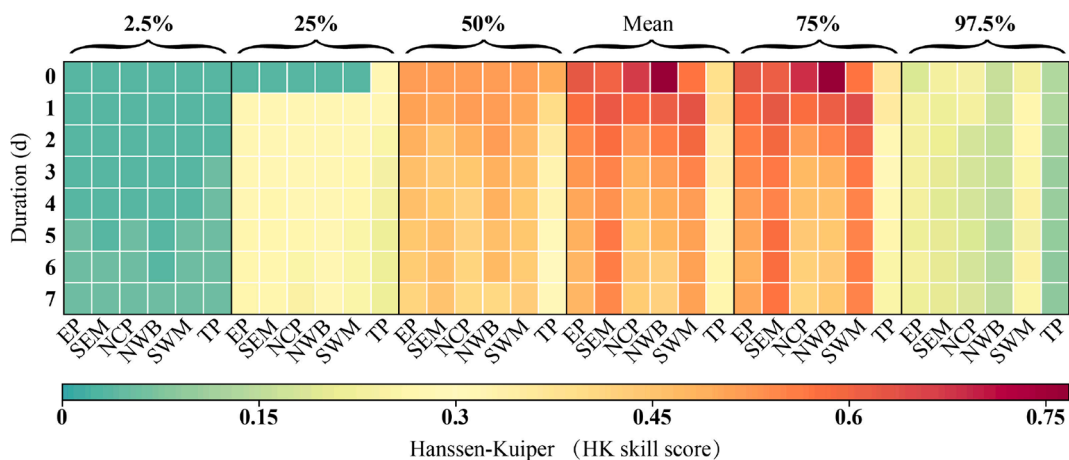

Fig. 11. The validation HK skill score on rainfall thresholds selection by using current daily rainfall and antecedent rainfall sequence.

Following the aforementioned criteria, the rainfall thresholds distinguishing between HMP and non-HMP were obtained accordingly (Table 4). Here, the final choices of rainfall thresholds in each geomorphic region were highlighted with red font and the values with accuracy values greater than 0.7 were labeled with bold. Ultimately, we obtained the rainfall thresholds with well performance in EP, SEM, and SWM. In SEM, the 1-day antecedent rainfall reach up to 22.9 mm was considered to reach the low triggering condition for HMP. In SWM, the critical value was detected as the 1-day antecedent rainfall of 15.5 mm. In EP, a HMP could be triggered when the rainfall in the current day

Table 4

Rainfall threshold values ($\tau_4 = 0.75$ without background or mean value with grey shade) for HMP initiation in six geomorphic-regions. Key: EP, eastern plains; SEM, southeastern hills; NCP, north-central plateaus; SWM, southwestern mountains; NWB, northwestern basins; TP, Tibetan Plateau. The final choices of rainfall thresholds in each geomorphic-region were highlighted with red font.

Duration（d）	EP	SEM	NCP	NWB	SWM	TP
Current rainfall	7.1	10.2	4.0	1.4	8. 4	5.3
1	16.6	22.9	9.2	2.6	15.5	9.9
2	23.5	34.9	14.2	3.5	20.8	13.8
3	28.8	45.1	17.6	4.2	25.7	17.4
4	32.6	53.0	20.7	4.8	29. 6	20.6
5	37.5	60.7	22.8	5.4	32.6	23.4
6	40.2	66.4	25.1	5.9	36.1	25.7
7	42.6	71.9	27.2	6.4	39.1	27.9

reaches 7.1 mm. The relationships between accumulative rainfall and duration shown in Fig. 12 presented the reference fitting lines for HMP triggering conditions in each geomorphic-region, and could be considered preliminary rainfall threhsolds. The equations obtained in SEM, SWM, EP, and TP showed a more reliable benchmark line. While, the low thresholds detected in NCP and NWB might partially due to the arid/semi-arid climatic conditions, which should be discussed with the further effort.

5. Discussions

5.1. Comparison with previous studies

The performance of GPM and CHIRPS have been evaluated via taking rain gauge observations as the benchmark over mainland China in several previous researches (e.g., Tan and Duan, 2017). Overall, GPM outperformed CHIRPS over the majority of the study area, except for the most northeast China. Despite the higher spatial resolution (0.05° × 0.05°) of CHIRPS, it indicated no big improvements in detecting the extreme rainfall events. As for GPM, the underestimation detected from daily rainfall may partially be attributed to the coarser spatial resolution (Khan and Maggioni, 2019). In spite of this, GPM showed the best performance in southern China, where conversely CHIRPS reported the most severe bias (Shen et al., 2020). Besides, GPM performed well for the detection of extreme events, such as R90p (see Fig. 4), indicating its applicability for capturing the rainfall responsible for HMP initiation. Smith et al. (1996) also observed that the intensity of some concentrated rainfall events can't be catched even by relatively dense rain gauge networks. For the specific analysis on HMP, which concentrated mostly in humid regions during the rainy season, it is a good choice to introduce

the GPM-derived rainfall indices into prediction on HMP. As an example, Tang et al. (2017) observed that the performance of GPM IMERG Late run are the closest to ground observations and recommended it in capturing HMP by taking the events of 2016 Summer in South China as an example. Similarly, Ma et al. (2020a) assessed the performance of GPM products in HMP warning in Yunnan province of China, and they confirmed that GPM IMERG Final run could contribute to improving the accuracy of HMP warning in their specific study area. Despite that the ability of satellite rainfall products on predicting HMP has been tested by researchers in several regions of China, these efforts either focus on a short time slice, or put an emphasis on the specific region. In this study, we gave the first try on deriving the rainfall thresholds by taking full use of the historical HMP records on a national scale. The empirical, statistical rainfall thresholds derived from antecedent rainfall series of HMP and non-HMP events represent the minimum rainfall conditions above which new HMP are likely to occurr, and could be considered as a preliminary reference.

In this work, the empirical rainfall triggering conditions for HMP within different geomorphological settings were defined taking full advantage of the duration of daily rainfall and a series of statistical cutoffs. The results suggested that the combination of these two parameters (*duration* and *cutoff*) should be adjusted with the shifting of background settings accordingly. The bimodal of the probability density plots displayed in Fig. 6b and 6e illustrated the apparent higher value detected in the longer period of accumulative rainfall. In regions located in semi-humid or semi-arid areas i.e. NCP, NWB, and TP, the antecedent rainfall with different durations showed little difference (Fig. 6c, 6d, and 6f). The most proper duration of antecedent rainfall for HMP occurrence in SEM and SWM were determined as 1 day, while for the other regions were defined as the current daily rainfall (red values in Table 4). This

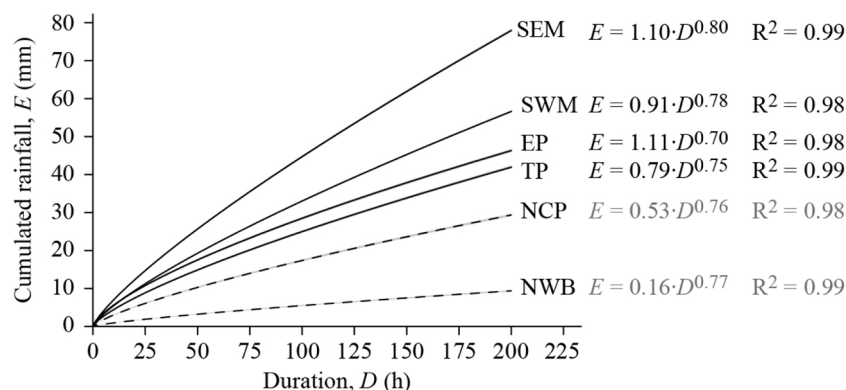**Fig. 12.** The rainfall thresholds for HMP initiation for the six geomorphic-regions. Dotted curves and equations in grey indicate not reliable thresholds.

SEM $E = 1.10 \cdot D^{0.80}$ $R^2 = 0.99$
SWM $E = 0.91 \cdot D^{0.78}$ $R^2 = 0.98$
EP $E = 1.11 \cdot D^{0.70}$ $R^2 = 0.98$
TP $E = 0.79 \cdot D^{0.75}$ $R^2 = 0.99$
NCP $E = 0.53 \cdot D^{0.76}$ $R^2 = 0.98$
NWB $E = 0.16 \cdot D^{0.77}$ $R^2 = 0.99$

could partially be attributed to that HMP occurrences in different geomorphic-regions encompass the diversity of meteorological and hydrological processes. Miao et al. (2016) defined and run an hydrological model based on geomorphological properties in four mountainous catchments ranging from humid to arid regions. They pointed out that in humid regions triggering conditions are related to long-time cumulative rainfall whereas in semi-humid and semi-arid regions they depend more on short-time rainfall events. Our findings shown in Fig. 6, 7, and Table 4 are in agreement with this argument in a broader context.

Besides, the traditional empirical method for the prediction of HMP initiation has also be tested by researchers. Here, we compared our findings with the results detected by He et al. (2020) and Ma et al. (2020b). The former proposed two groups of rainfall thresholds: the cumulated event rainfall duration thresholds (*E-D*) by using merged and CMORPH rainfall products. For instance, the *E-D* in the rainy season in their work were defined as $E = 0.86D^{0.48}(1h \leqslant D \leq 47h)$ and $E = 0.18D^{1.07}(48h \leqslant D \leqslant 602h)$. Moreover, Ma et al. (2020b) proposed a rainfall trigger index for selecting early warning methods in the light of trigger factors. They obtained the fitting relationship between rainfall intensity and duration (*I-D*): $I = 16D^{-0.7}$, for Yunnan province (located in Southwest China). Similarly, we achieved the relationship between accumulative rainfall and duration indicating that $E = 0.91D^{0.78}$ in the same region (region SWM), as well as the targeted relationships in the other geomorphic-regions across the entire Chinese territory (see Fig. 12). However, it should be acknowledged that the thresholds defined by He et al. (2020) are related only to landslides initiation, and the work by Ma et al. (2020b) focused purely on the flash floods in a small sector of China, while the thresholds defined in our work are related to the wide spectrum of all hydro-morphological processes (HMP) across the entire Chinese territory. Therefore, a direct comparison among them could be not very rigorous, also because the methods used for their calculations are different. In particular, the method here proposed is based on the cutoff between HMP and non-HMP triggering conditions and on the HK discriminant, so guaranteeing a better compromise between correct and incorrect predictions. However, if we compare the threshold values of a cumulated rainfall with a duration of 24 h, we observe that the values here calculated for all geomorphic-regions (only reliable thresholds) are lower than the value obtained by Ma et al. (2020b) for a sector of China and by far higher than the value obtained by He et al. (2020) for the whole Chinese territory.

5.2. Uncertainties and limitations

The rapid rise and the continuous update of satellite rainfall products offer interesting chances for hydro-morphological studies (Hapuarachchi et al., 2011) and for the definition of triggering conditions of geo-hydrological and hydro-morphological processes. This work took full advantage of these challenges by combining satellite-based datasets with geomorphological settings as input. Satellite-based rainfall estimates offer good solutions, with pros and cons (e.g., significant estimation uncertainties in some cases), to the coarse density of ground measuring instruments at the national to continental to global scale (Nikolopoulos et al., 2017). In some cases, e.g. in data scarce regions, satellite rainfall products are the only available data source. The use of satellite rainfall products is becoming very popular among scientists and technicians working on geo-hydrological and hydro-morphological analyses, and their resolution is surely a relevant issue when rainfall estimates are used in such analyses. However, in the present case (i.e. the whole Chinese territory) the grid resolution is lower than the average reference area of each rain gauge included in the available network.

Commonly, satellite-based rainfall products can provide pixel-level spatial average measurement results (compared to a punctual larger spatial rainfall intensity retrievable from rain gauges). As also stated by Brunetti et al. (2018), such underestimation could result in bias for rainfall thresholds, e.g. low threshold values as some derived in this

work. The coarse spatial resolution of satellite rainfall products would also lead to the restricted depiction on the spatial heterogeneous rainfall patterns (Chikalamo et al., 2020). However, the rainfall product performance in terms of its ability to detect rainfall events leading to HMPs is not affected, in particular if the products are not biased in space and time (Brunetti et al., 2018), as the case of used products.

Concerning rainfall thresholds, those defined in this work should also be considered with respect to the associated topographic attributes, soil types, and vegetation coverage to getting the more robust prediction. The historical HMP inventory used in this study provided a large amount of records for the empirical estimation, however, still far from completeness, which could also lead to uncertainties. Another source of uncertainties in the thresholds is to be found in the coarse temporal resolution of daily rainfall data of some products (Gariano et al., 2020). Additionally, the statistically-based method proposed in this study did not pay attention to the possibility of temporal non-stationary inherited from climate change (e.g. Seidou et al., 2012; Salas and Obeysekera, 2014). Finally, we estimated the rainfall thresholds over a large area, which might result in the uncertainties due to the complex environmental settings. However, our main aim was to provide some new insight into assessing the rainfall triggering conditions by taking full advantage of satellite rainfall products together with long-term historical HMP records. We suggested to perform this practically easy and straightforward approach within a catchment scale to obtain and update the rainfall triggering conditions with a finer spatio-temporal resolution.

6. Conclusion

In this work, an empirical, statistically-based method to detect the rainfall conditions for the initiation of hydro-morphological processes (HMP), based on satellite rainfall datasets and long-term historical catalogue is proposed. The quantile relationship of the antecedent rainfall for HMP/non-HMP were established for detecting the reliable rainfall triggering conditions. The results verified the ability of satellite-derived rainfall indices to provide a preliminary reference for HMP prediction. We list the main conclusions drawn from this work below:

1. GPM outperformed CHIRPS products at deriving the daily rainfall by setting ground rain gauge observations as reference. The best performance of satellite rainfall products were detected in southern China, and higher bias were prone to show in arid regions. These two products both had a higher consistency with gauge measurements for extreme indices, with the highest accuracy for R90p.
2. Current daily rainfall calculated via GPM indicated the severe underestimation versus the grid-interpolated rain gauge rainfall estimates on capturing HMP. The high value of relative bias between these two datasets is homogeneously distribution in spatial.
3. The rainfall triggering conditions and the preliminary rainfall thresholds for HMP initiation were determined by using a series of antecedent rainfall within different geomorphic-regions. The cutoffs were setting as $\tau_4 = 0.75$ and mean value of 1-day antecedent rainfall in SEM and SWM, respectively. While, the $\tau_4 = 0.75$ or mean values of the current daily rainfall work better in EP, NCP, and NWB.

We maintain that the thresholds here defined can provide good results in an operational application, for different reasons: first, the applied method, based on the cutoff between HMP and non-HMP conditions and on the HK discriminant, guarantees a good compromise between correct and incorrect predictions - this is not the case of the other mentioned studies in China; second, the use of daily rainfall data to reconstruct triggering rainfall events can produce high uncertainties in the threshold parameters - this can be overcome when using fixed duration values, as in the present case; third, the validity range of the thresholds here defined is up to 7 days, which is a reasonable duration of a rainfall event responsible for the triggering of a hydro-morphological process - on the contrary, longer duration ranges, as defined in the other

works, include rainfall events too long for the initiation of a shallow landslide or a flash flood. Finally, the here defined thresholds refer to a catalog that encompasses the whole spectrum of phenomena defined as hydro-morphological processes; this can represent another strength in an operational application, given that the occurrence of different phenomena triggered by rainfall (e.g. shallow landslides, debris flows, flash floods) can have similar effects on an element at risk (e.g. population, properties, infrastructures); therefore, their concurrent prediction that can be achieved with the proposed models is useful for civil protection purposes.

This work made an attempt on detecting the rainfall triggering conditions of HMP within different geomorphological settings, which has not yet been implemented on a national scale in China. This could be utilized as a guideline for HMP risk management in China. A potential improvement of our work might be a further downscaling of the analysis and the spatial distribution of the rainfall thresholds, which currently are only related to six, wide geomorphic-regions. Moreover, the bias and uncertainties might also be discussed in terms of the complex localized terrain and climate. We addressed that the absolute rainfall value obtained from multi-sources should not be compared directly. The method for determining rainfall triggering conditions from satellite rainfall products also ought to be applied in similar contexts.

CRediT authorship contribution statement

Nan Wang: Conceptualization, Methodology, Writing - Original Draft; **Weiming Cheng**: Conceptualization and Supervision; **Luigi Lombardo** and **Stefano Luigi Gariano**: Writing - Review & Editing; **Changjun Liu**: Supervision and Funding acquisition; **Junnan Xiong** and **Ruibo Wang**: Supervision.

Declaration of Competing Interest

The authors declare that they have no known competing financial interests or personal relationships that could have appeared to influence the work reported in this paper.

Acknowledgement

Appendix A. Supplementary material

Supplementary data associated with this article can be found, in the online version, at https://doi.org/10.1016/j.jag.2021.102350.

References

Abancó, C., Hürlimann, M., Moya, J., Berenguer, M., 2016. Critical rainfall conditions for the initiation of torrential flows. Results from the Rebaixader catchment (Central Pyrenees). J. Hydrol. 541, 218–229.

Amato, G., Eisank, C., Castro-Camilo, D., Lombardo, L., 2019. Accounting for covariate distributions in slope-unit-based landslide susceptibility models. A case study in the alpine environment. Eng. Geol. 260, 105237.

Ashouri, H., Nguyen, P., Thorstensen, A., Hsu, K.-L., Sorooshian, S., Braithwaite, D., 2016. Assessing the efficacy of high-resolution satellite-based PERSIANN-CDR precipitation product in simulating streamflow. J. Hydrometeorol. 17 (7), 2061–2076.

Badoux, A., Turowski, J., Mao, L., Mathys, N., Rickenmann, D., 2012. Rainfall intensity–duration thresholds for bedload transport initiation in small Alpine watersheds. Nat. Hazards Earth Syst. Sci. 21, 3091–3108.

Bai, L., Shi, C., Li, L., Yang, Y., Wu, J., 2018. Accuracy of CHIRPS satellite-rainfall products over mainland China. Remote Sens. 10 (3), 362.

Bai, S., Wang, J., Thiebes, B., Cheng, C., Yang, Y., 2014. Analysis of the relationship of landslide occurrence with rainfall: a case study of Wudu County, China. Arab. J. Geosci. 7 (4), 1277–1285.

Bezak, N., Šraj, M., Mikoš, M., 2016. Copula-based IDF curves and empirical rainfall thresholds for flash floods and rainfall-induced landslides. J. Hydrol. 541, 272–284.

Blanchard, B.J., McFarland, M.J., Schmugge, T.J., Rhoades, E., 1981. Estimation of soil moisture with API algorithms and microwave emission 1. JAWRA J. Am. Water Resour. Assoc. 17 (5), 767–774.

Borga, M., Stoffel, M., Marchi, L., Marra, F., Jakob, M., 2014. Hydrogeomorphic response to extreme rainfall in headwater systems: flash floods and debris flows. J. Hydrol. 518, 194–205.

Bout, B., Lombardo, L., van Westen, C.J., Jetten, V.G., 2018. Integration of two-phase solid fluid equations in a catchment model for flash floods, debris flows and shallow slope failures. Environ. Model. Softw. 105, 1–16.

Brunetti, M.T., Melillo, M., Peruccacci, S., Ciabatta, L., Brocca, L., 2018. How far are we from the use of satellite rainfall products in landslide forecasting? Remote Sens. Environ. 210, 65–75.

Chikalamo, E.E., Mavrouli, O.C., Ettema, J., van Westen, C.J., Muntohar, A.S., Mustofa, A., 2020. Satellite-derived rainfall thresholds for landslide early warning in Bogowonto Catchment, Central Java, Indonesia. Int. J. Appl. Earth Obs. Geoinf. 89, 102093.

Creutin, J.-D., Borga, M., 2003. Radar hydrology modifies the monitoring of flash-flood hazard. Hydrol. Process. 17 (7), 1453–1456.

Doswell III, C.A., Brooks, H.E., Maddox, R.A., 1996. Flash flood forecasting: An ingredients-based methodology. Weather Forecast. 11 (4), 560–581.

Fang, J., Yang, W., Luan, Y., Du, J., Lin, A., Zhao, L., 2019. Evaluation of the TRMM 3B42 and GPM IMERG products for extreme precipitation analysis over China. Atmos. Res. 223, 24–38.

Fawcett, T., 2006. An introduction to ROC analysis. Pattern Recogn. Lett. 27 (8), 861–874.

Funk, C., Peterson, P., Landsfeld, M., Pedreros, D., Verdin, J., Shukla, S., Husak, G., Rowland, J., Harrison, L., Hoell, A., et al., 2015. The climate hazards infrared precipitation with stations—a new environmental record for monitoring extremes. Sci. Data 2 (1), 1–21.

Funk, C.C., Peterson, P.J., Landsfeld, M.F., Pedreros, D.H., Verdin, J.P., Rowland, J.D., Romero, B.E., Husak, G.J., Michaelsen, J.C., Verdin, A.P., et al., 2014. A quasi-global precipitation time series for drought monitoring. US Geol. Surv. Data Ser. 832 (4), 1–12.

Gao, Z., Long, D., Tang, G., Zeng, C., Huang, J., Hong, Y., 2017. Assessing the potential of satellite-based precipitation estimates for flood frequency analysis in ungauged or poorly gauged tributaries of China's Yangtze River basin. J. Hydrol. 550, 478–496.

Gariano, S.L., Melillo, M., Peruccacci, S., Brunetti, M.T., 2020. How much does the rainfall temporal resolution affect rainfall thresholds for landslide triggering? Nat. Hazards 100, 655–670.

Glade, T., Crozier, M., Smith, P., 2000. Applying probability determination to refine landslide-triggering rainfall thresholds using an empirical Antecedent Daily Rainfall Model. Pure Appl. Geophys. 157 (6), 1059–1079.

Green, D., Swets, J., 1966. Signal detection theory and psychophysics. John Wiley and Sons, New York, ISBN 0-471-32420-5.

Gupta, V., Jain, M.K., Singh, P.K., Singh, V., 2020. An assessment of global satellite-based precipitation datasets in capturing precipitation extremes: A comparison with observed precipitation dataset in India. Int. J. Climatol. 40 (8), 3667–3688.

Hanssen, A., Kuipers, W., 1965. On the relationship between rain and various meteorological parameters. (with reference to the problem of objective forecasting). Koninklijk Nederlands Meteorologisch Instituut.

Hapuarachchi, H., Wang, Q., Pagano, T., 2011. A review of advances in flash flood forecasting. Hydrol. Process. 25 (18), 2771–2784.

Hartke, S.H., Wright, D.B., Kirschbaum, D.B., Stanley, T.A., Li, Z., 2020. Incorporation of satellite precipitation uncertainty in a landslide hazard nowcasting system. J. Hydrometeorol. 21 (8), 1741–1759.

He, S., Wang, J., Liu, S., 2020. Rainfall event–duration thresholds for landslide occurrences in China. Water 12 (2), 494.

Hong, Y., Adler, R., Negri, A., Huffmann, G., 2007. Flood and landslide applications of near real-time satellite rainfall products. Nat. Hazards 43, 285–294.

Hosmer, D.W., Lemeshow, S., 2000. Applied logistic regression. Wiley Publishing.

Hou, A.Y., Kakar, R.K., Neeck, S., Azarbarzin, A.A., Kummerow, C.D., Kojima, M., Oki, R., Nakamura, K., Iguchi, T., 2014. The global precipitation measurement mission. Bull. Am. Meteorol. Soc. 95 (5), 701–722.

Huffman, G.J., Adler, R.F., Arkin, P., Chang, A., Ferraro, R., Gruber, A., Janowiak, J., McNab, A., Rudolf, B., Schneider, U., 1997. The global precipitation climatology project (GPCP) combined precipitation dataset. Bull. Am. Meteor. Soc. 78 (1), 5–20.

Huffman, G.J., Adler, R.F., Morrissey, M.M., Bolvin, D.T., Curtis, S., Joyce, R., McGavock, B., Susskind, J., 2001. Global precipitation at one-degree daily resolution from multisatellite observations. J. Hydrometeorol. 2 (1), 36–50.

Huffman, G.J., Bolvin, D.T., Nelkin, E.J., et al., 2015. Integrated Multi-satellitE Retrievals for GPM (IMERG) technical documentation. NASA/GSFC Code 612, 47.

Huffman, G.J., Bolvin, D.T., Nelkin, E.J., Wolff, D.B., Adler, R.F., Gu, G., Hong, Y., Bowman, K.P., Stocker, E.F., 2007. The TRMM multisatellite precipitation analysis (TMPA): Quasi-global, multiyear, combined-sensor precipitation estimates at fine scales. J. Hydrometeorol. 8 (1), 38–55.

Jia, G., Tang, Q., Xu, X., 2020. Evaluating the performances of satellite-based rainfall data for global rainfall-induced landslide warnings. Landslides 17, 283–299.

Jiang, L., Bauer-Gottwein, P., 2019. How do GPM IMERG precipitation estimates perform as hydrological model forcing? Evaluation for 300 catchments across Mainland China. J. Hydrol. 572, 486–500.

Jollifee, I., Stephenson, D., 2003. Forecast verification. A practitioner's guide in atmospheric science. John Wiley, Chichester.

Joyce, R.J., Janowiak, J.E., Arkin, P.A., Xie, P., 2004. CMORPH: A method that produces global precipitation estimates from passive microwave and infrared data at high spatial and temporal resolution. J. Hydrometeorol. 5 (3), 487–503.

Khan, S., Maggioni, V., 2019. Assessment of level-3 gridded Global Precipitation Mission (GPM) products over oceans. Remote Sens. 11 (3), 255.

Kirschbaum, D., Stanley, T., 2018. Satellite-based assessment of rainfall-triggered landslide hazard for situational awareness. Earth's Future 6 (3), 505–523.

Kirschbaum, D., Stanley, T., Simmons, S., 2015. A dynamic landslide hazard assessment system for Central America and Hispaniola. Nat. Hazards Earth Syst. Sci. 15, 2257–2272.

Klein Tank, A., Zwiers, A., Zhang, X., 2009. Guidelines on analysis of extremes in a changing climate in support of informed decisions for adaptation. World Meteorol. Organiz.

Kohler, M.A., Linsley, R.K., 1951. Predicting the runoff from storm rainfall, vol. 30. US Department of Commerce, Weather Bureau.

Kubota, T., Shige, S., Hashizume, H., Aonashi, K., Takahashi, N., Seto, S., Hirose, M., Takayabu, Y.N., Ushio, T., Nakagawa, K., et al., 2007. Global precipitation map using satellite-borne microwave radiometers by the GSMaP project: Production and validation. IEEE Trans. Geosci. Remote Sens. 45 (7), 2259–2275.

Liu, Y., Yang, Z., Huang, Y., Liu, C., 2018. Spatiotemporal evolution and driving factors of China's flash flood disasters since 1949. Sci. China Earth Sci. 61 (12), 1804–1817.

Lombardo, L., Mai, P.M., 2018. Presenting logistic regression-based landslide susceptibility results. Eng. Geol. 244, 14–24.

Lombardo, L., Opitz, T., Ardizzone, F., Guzzetti, F., Huser, R., 2020. Space-time landslide predictive modelling. Earth-Sci. Rev. 103318.

Ma, M., Wang, H., Jia, P., Tang, G., Wang, D., Ma, Z., Yan, H., 2020a. Application of the GPM-IMERG Products in Flash Flood Warning: A Case Study in Yunnan, China. Remote Sens. 12 (12), 1954.

Ma, M., Wang, H., Yang, Y., Zhao, G., Tang, G., Hong, Z., Clark III, R.A., Chen, Y., Xu, H., Hong, Y., 2020b. Development of a new rainfall-triggering index of flash flood warning-case study in Yunnan province, China. J. Flood Risk Manage. e12676.

Ma, T., Li, C., Lu, Z., Wang, B., 2014. An effective antecedent precipitation model derived from the power-law relationship between landslide occurrence and rainfall level. Geomorphology 216, 187–192.

Miao, Q., Yang, D., Yang, H., Li, Z., 2016. Establishing a rainfall threshold for flash flood warnings in China's mountainous areas based on a distributed hydrological model. J. Hydrol. 541, 371–386.

Monsieurs, E., Dewitte, O., Depicker, A., Demoulin, A., 2019. Towards a transferable antecedent rainfall—susceptibility threshold Approach for Landsliding. Water 11 (11), 2202.

Nikolopoulos, E., Borga, M., Creutin, J., Marra, F., 2015. Estimation of debris flow triggering rainfall: influence of rain gauge density and interpolation methods. Geomorphology 243, 40–50.

Nikolopoulos, E., Crema, S., Marchi, L., Marra, F., Guzzetti, F., Borga, M., 2014. Impact of uncertainty in rainfall estimation on the identification of rainfall thresholds for debris flow occurrence. Geomorphology 221, 286–297.

Nikolopoulos, E.I., Destro, E., Maggioni, V., Marra, F., Borga, M., 2017. Satellite rainfall estimates for debris flow prediction: An evaluation based on rainfall accumulation–duration thresholds. J. Hydrometeorol. 18 (8), 2207–2214.

Norbiato, D., Borga, M., Degli Esposti, S., Gaume, E., Anquetin, S., 2008. Flash flood warning based on rainfall thresholds and soil moisture conditions: An assessment for gauged and ungauged basins. J. Hydrol. 362 (3–4), 274–290.

Rahmati, O., Kornejady, A., Samadi, M., Deo, R.C., Conoscenti, C., Lombardo, L., Dayal, K., Taghizadeh-Mehrjardi, R., Pourghasemi, H.R., Kumar, S., et al., 2019. PMT: New analytical framework for automated evaluation of geo-environmental modelling approaches. Sci. Total Environ. 664, 296–311.

Ramos Filho, G.M., Coelho, V.H.R., da Silva Freitas, E., Xuan, Y., das Neves Almeida, C., 2020. An improved rainfall-threshold approach for robust prediction and warning of flood and flash flood hazards. Nat. Hazards 1–21.

Rossi, M., Kirschbaum, D., Valigi, D., Mondini, A., Guzzetti, F., 2017. Comparison of satellite rainfall estimates and rain gauge measurements in Italy, and impact on landslide modeling. Climate 5 (4).

Salas, J., Obeysekera, J., 2014. Revisiting the concepts of return period and risk for nonstationary hydrologic extreme events. J. Hydrol. Eng. 19, 554–568.

Salles, L., Satgé, F., Roig, H., Almeida, T., Olivetti, D., Ferreira, W., 2019. Seasonal effect on spatial and temporal consistency of the New GPM-Based IMERG-v5 and GSMaP-v7 satellite precipitation estimates in Brazil's central plateau egion. Water 11 (4), 668.

Saunders, K., Stephenson, A.G., Taylor, P.G., Karoly, D., 2017. The spatial distribution of rainfall extremes and the influence of El Niño Southern Oscillation. Weather Climate Extremes 18, 17–28.

Schlather, M., 2002. Models for stationary max-stable random fields. Extremes 5 (1), 33–44.

Schlögel, R., Kofler, C., Gariano, S., Van Campenhout, J., Plummer, S., 2020. Changes in climate patterns and their association to natural hazard distribution in South Tyrol (Eastern Italian Alps). Sci. Rep. 10, 5022.

Scofield, R.A., Kuligowski, R.J., 2003. Status and outlook of operational satellite precipitation algorithms for extreme-precipitation events. Weather Forecast. 18 (6), 1037–1051.

Seidou, O., Ramsay, A., Nistor, I., 2012. Climate change impacts on extreme floods I: combining imperfect deterministic simulations and non-stationary frequency analysis. Nat. Hazards Earth Syst. Sci. 61, 647–659.

Seneviratne, S., Nicholls, N., Easterling, D., Goodess, C., Kanae, S., Kossin, J., Luo, Y., Marengo, J., McInnes, K., Rahimi, M., Reichstein, M., Sorteberg, A., Vera, C., Zhang, X., 2012. Changes in climate extremes and their impacts on the natural physical environment. Cambridge University Press, Cambridge, UK, and New York, NY, USA, pp. 109–230.

Shen, Z., Yong, B., Gourley, J.J., Qi, W., Lu, D., Liu, J., Ren, L., Hong, Y., Zhang, J., 2020. Recent global performance of the Climate Hazards group Infrared Precipitation (CHIRP) with Stations (CHIRPS). J. Hydrol. 125284.

Smith, J.A., Seo, D.J., Baeck, M.L., Hudlow, M.D., 1996. An intercomparison study of NEXRAD precipitation estimates. Water Resour. Res. 32 (7), 2035–2045.

Sorooshian, S., Hsu, K.-L., Gao, X., Gupta, H.V., Imam, B., Braithwaite, D., 2000. Evaluation of PERSIANN system satellite-based estimates of tropical rainfall. Bull. Am. Meteorol. Soc. 81 (9), 2035–2046.

Stephenson, D.B., 2000. Use of the odds ratio for diagnosing forecast skill. Weather Forecast. 15 (2), 221–232.

Su, J., Lü, H., Ryu, D., Zhu, Y., 2019. The assessment and comparison of TMPA and IMERG products over the major basins of Mainland China. Earth Space Sci. 6 (12), 2461–2479.

Sungmin, O., Foelsche, U., Kirchengast, G., Fuchsberger, J., Tan, J., Petersen, W.A., 2017. Evaluation of GPM IMERG Early, Late, and Final rainfall estimates using WegenerNet gauge data in southeastern Austria. Hydrol. Earth Syst. Sci. 21 (12).

Tan, M.L., Duan, Z., 2017. Assessment of GPM and TRMM precipitation products over Singapore. Remote Sens. 9 (7), 720.

Tang, G., Clark, M.P., Papalexiou, S.M., Ma, Z., Hong, Y., 2020. Have satellite precipitation products improved over last two decades? A comprehensive comparison of GPM IMERG with nine satellite and reanalysis datasets. Remote Sens. Environ. 240, 111697.

Tang, G., Zeng, Z., Ma, M., Liu, R., Wen, Y., Hong, Y., 2017. Can near-real-time satellite precipitation products capture rainstorms and guide flood warning for the 2016 summer in south china? IEEE Geosci. Remote Sens. Lett. 14 (8), 1208–1212.

Tegmark, M., Wu, T., 2020. Pareto-optimal data compression for binary classification tasks. Entropy 22 (1), 7.

Toté, C., Patricio, D., Boogaard, H., Van der Wijngaart, R., Tarnavsky, E., Funk, C., 2015. Evaluation of satellite rainfall estimates for drought and flood monitoring in Mozambique. Remote Sens. 7 (2), 1758–1776.

Viessman, W., Lewis, G.L., Knapp, J.W., Harbaugh, T.E., 1989. Introduction to hydrology. Harper & Row New York.

Vrugt, J.A., Gupta, H.V., Bastidas, L.A., Bouten, W., Sorooshian, S., 2003. Effective and efficient algorithm for multiobjective optimization of hydrologic models. Water Resour. Res. 39 (8).

Wang, N., Cheng, W., Wang, B., Liu, Q., Zhou, C., 2020. Geomorphological regionalization theory system and division methodology of China. J. Geog. Sci. 30 (2), 212–232.

Wang, Z., Zhong, R., Lai, C., Chen, J., 2017. Evaluation of the GPM IMERG satellite-based precipitation products and the hydrological utility. Atmos. Res. 196, 151–163.

Wei, F., Hu, K., Zhang, J., Jiang, Y., Chen, J., 2008. Determination of effective antecedent rainfall for debris flow forecast based on soil moisture content observation in Jiangjia Gully, China. In: DeWrachien, D., Brebbia, C.A., Lenzi, M.A. (Eds.), Monitoring, Simulation, Prevention and Remediation of Dense Debris Flows II. pp. 13–22.

Wilks, D.S., 2011. Statistical methods in the atmospheric sciences, vol. 100. Academic Press.

Yuan, F., Zhang, L., Soe, K.M.W., Ren, L., Zhao, C., Zhu, Y., Jiang, S., Liu, Y., 2019. Applications of TRMM-and GPM-Era multiple-satellite precipitation products for flood simulations at sub-daily scales in a sparsely gauged watershed in Myanmar. Remote Sens. 11 (2), 140.

Zhou, Z., Guo, B., Xing, W., Zhou, J., Xu, F., Xu, Y., 2020. Comprehensive evaluation of latest GPM era IMERG and GSMaP precipitation products over mainland China. Atmos. Res. 105132.